HD 143006: circumbinary planet or misaligned disc?

G. Ballabio,[1,2]★ R. Nealon [iD],[2,3,4] R. D. Alexander [iD],[2] N. Cuello,[5] C. Pinte [iD][5,6] and D. J. Price [iD][6]

[1]*Astronomy Unit, School of Physics and Astronomy, Queen Mary University of London, Mile End Road, London E1 4NS, UK*
[2]*School of Physics and Astronomy, University of Leicester, Leicester LE1 7RH, UK*
[3]*Centre for Exoplanets and Habitability, University of Warwick, Coventry CV4 7AL, UK*
[4]*Department of Physics, University of Warwick, Coventry CV4 7AL, UK*
[5]*IPAG, CNRS, Univ. Grenoble Alpes, F-38000 Grenoble, France*
[6]*School of Physics and Astronomy, Monash University, Clayton, VIC 3800, Australia*

ABSTRACT

Misalignments within protoplanetary discs are now commonly observed, and features such as shadows in scattered light images indicate departure from a co-planar geometry. VLT/SPHERE (Very Large Telescope/Spectro-Polarimetric High-contrast Exoplanet REsearch) observations of the disc around HD 143006 show a large-scale asymmetry and two narrow dark lanes that are indicative of shadowing. ALMA (Atacama Large Millimeter/submillimeter Array) observations also reveal the presence of rings and gaps in the disc, along with a bright arc at large radii. We present new hydrodynamic simulations of HD 143006, and show that a configuration with both a strongly inclined binary and an outer planetary companion is the most plausible to explain the observed morphological features. We compute synthetic observations from our simulations, and successfully reproduce both the narrow shadows and the brightness asymmetry seen in infrared scattered light. Additionally, we reproduce the large dust observed in the mm continuum, due to a 10 Jupiter-mass planet detected in the CO kinematics. Our simulations also show the formation of a circumplanetary disc, which is misaligned with respect to the outer disc. The narrow shadows cast by the inner disc and the planet-induced 'kink' in the disc kinematics are both expected to move on a time-scale of $\sim$5–10 yr, presenting a potentially observable test of our model. If confirmed, HD 143006 would be the first known example of a circumbinary planet on a strongly misaligned orbit.

Key words: accretion, accretion discs – hydrodynamics – methods: numerical – protoplanetary discs.

1 INTRODUCTION

High angular resolution observations at multiple wavelengths have shown a wealth of substructures within protoplanetary discs, such as ring-like features, horseshoes, spirals, and other azimuthal asymmetries (e.g. ALMA Partnership 2015; Andrews 2020; Francis & van der Marel 2020), which are detected in both the optical/NIR and (sub-)millimetre regimes. While sub-mm and mm observations mostly probe the disc mid-plane, near-IR (NIR) observations trace the surface layers of the disc.

The focus of this paper is the protoplanetary disc around the T Tauri star HD 143006. The central object is a G-type star, with temperature $T_{\rm eff} = 5880$ K, luminosity $L_* = 4.58$ L$_\odot$, and mass $M_* = 1.8^{+0.2}_{-0.3}$ M$_\odot$ (Andrews et al. 2018; Benisty et al. 2018). It is located at a distance of 165 $\pm$ 5 pc (Gaia Collaboration 2018), in the region of Upper Sco, and it is relatively old (4–12 Myr; Pecaut, Mamajek & Bubar 2012). Non-detections in interferometric (Kraus et al. 2008) and high-contrast imaging (Benisty et al. 2018) observations set an upper limit on the mass of the companion to be $\sim$0.4 M$_\odot$. This corresponds to a limit on the mass ratio of any putative binary of $q \lesssim 0.2$. Any objects more massive than this should have been detected in the infrared (IR). Additionally, disc structures in the polarized scattered

light image are resolved down to an angular separation of $\sim$0.06 arcsec. For any binary separation smaller than $\sim$10 au, it would not be possible to distinguish the two stars.

The disc around HD 143006 is seen close to face-on, and has recently been studied in detail at multiple wavelengths. Benisty et al. (2018) presented polarized scattered light J-band images observed with Very Large Telescope (VLT)/Spectro-Polarimetric High-contrast Exoplanet REsearch (SPHERE), with an angular resolution of $\sim$0.037 arcsec (6.1 au). HD 143006 has also been observed at very high resolution (0.046 arcsec, i.e. 7.6 au) as part of the Disc Substructures at High Angular Resolution Project (DSHARP) survey (Andrews et al. 2018) and its 1.25-mm continuum emission has been analysed by Pérez et al. (2018).

The origin of most of the structures visible in the disc is not yet fully understood. Here, we briefly summarize the main detected morphological features:

(i) The IR scattered light image shows an asymmetric ring-like feature between 18 and 30 au that presents two narrow shadows along the north–south direction. A broader dark region, covering the western half of the disc, can also be seen (Benisty et al. 2018).

(ii) The SPHERE image also shows an overbrightness at about PA $\sim$ 150° (Benisty et al. 2018).

(iii) The scattered light observations imply a relative misalignment of $\sim$30° between the inner and outer discs (Benisty et al. 2018).

★ E-mail: g.ballabio@qmul.ac.uk

(iv) The 1.3-mm continuum emission from the disc resolves into three bright rings at roughly 8, 40, and 64 au from the disc centre, and a large gap between ∼10 and 30 au (Andrews et al. 2018; Pérez et al. 2018).

(v) A bright arc in the south-east is also visible in the dust observations, outside of the outermost ring at ∼74 au (Andrews et al. 2018; Pérez et al. 2018).

(vi) Kinematic observations of the CO line reveal a 'kink' in the redshifted channel that is not present in the blueshifted channel (Andrews et al. 2018; Pérez et al. 2018; Pinte et al. 2020).

Most of these substructures suggest that the inner disc is misaligned, which could be due to either a central binary or a planet located further out in the disc. Previous 3D hydrodynamic simulations have already shown that an inclined binary causes disc breaking (e.g. Facchini, Lodato & Price 2013; Nixon, King & Price 2013), producing azimuthal asymmetries in scattered light observations (e.g. Facchini, Juhász & Lodato 2018; Montesinos & Cuello 2018; Nealon, Price & Pinte 2020). Indeed, the disc breaks into two distinct components, with the resulting inner disc misaligned with respect to the outer regions. The inner disc precesses as a rigid body while the outer disc evolves similarly on a longer time-scale. Such a configuration produces a unique signature in IR observations. The light of the star is blocked by the inner disc, which is optically thick to such wavelengths and casts a shadow on to the outer disc. The morphology of the SPHERE image of HD 143006 was approximately recovered using 3D hydrodynamic simulations of a disc warped by a misaligned equal-mass binary (Benisty et al. 2018; Facchini et al. 2018), though such a massive companion is ruled out by existing IR observations (Kraus et al. 2008; Benisty et al. 2018).

Alternatively, a misaligned planetary companion has been suggested to help explain the disc structure. Such a planet would have a mass equal to 10–100 M_{Jup} (i.e. mass ratio 0.01–0.1), potentially located between 8 and 40 au. As suggested by Benisty et al. (2018), for example, a 10 Jupiter-mass planet around a 1.5 $M_{\odot}$ star would not be detected by interferometric observations and, at the same time, may cause the misalignment of an inner disc. The hypothesis of a planet-hosting disc is strongly suggested by the ALMA dust continuum image, which shows a large gap at about ∼22 au. As already inferred by Zhang et al. (2018), an embedded object with a mass of about ∼10–20 M_{Jup} could easily produce a dust depletion as expected in the sub-mm observations. Moreover, Pérez et al. (2018) analysed the CO emission and found a deviation from the Keplerian rotation pattern in the redshifted channels, at a radial distance of about 32 au. This, again, hints at the presence of a planetary companion, within the annular dust gap. Pinte et al. (2019) showed that embedded planets perturb the disc gas, resulting in a kinematic signature that is detectable with high-resolution observations. They found that the minimum detectable mass in kinematic observations is roughly 2 M_{Jup}. In a kinematic study of multiple sources within the DSHARP sample, Pinte et al. (2020) found that HD 143006 has significantly larger velocity perturbations than the other sources, which points towards the presence of a planet more massive than 1–3 M_{Jup}.

The combination of the previous configurations has never been considered so far. If existent, it would imply a planet orbiting a binary. In this scenario, planets are generally classified as S-type and P-type planets depending on the perturbation induced by the host stars. S-type (or circumstellar) planets orbit around one of the stars of the system, while P-type (or circumbinary) planets orbit around both stars. The occurrence rate of the two populations is very different, where more than 120 are known as circumstellar planets while only a dozen are circumbinary planets (Marzari & Thebault

2019). Additionally, planets around binary stars may have their orbits inclined with respect to that of the binary. This explanation has been invoked to interpret systems like 16 Cygn B. The eccentric planet was initially thought to be on a circular inclined orbit, which then became aligned and eccentric due to Kozai–Lidov oscillations (Holman, Touma & Tremaine 1997). Systematic studies looking at the stability of S-type planets are being developed, considering the properties of the binary as well as the planet distance and inclination (e.g. Quarles et al. 2020). On the contrary, similar studies for P-type planets have not been exploited so far.

We will show in this paper that a single companion, of either stellar or planetary mass, cannot account for the bright arc seen in both the SPHERE (ii) and ALMA (v) observations at about the same azimuthal location, but different radii. In this paper, we reconsider both of these scenarios, and their limitations, and instead propose that the HD 143006 disc hosts both a misaligned stellar binary and a giant circumbinary planet.

2 NUMERICAL METHODS

We perform 3D hydrodynamic simulations using the smoothed particle hydrodynamics (SPH) code PHANTOM (Price et al. 2018a). We perform a suite of numerical simulations to investigate scenarios to explain the morphological features observed in the disc surrounding HD 143006. Common to all our simulations, we model a gaseous disc of mass 0.01 $M_{\odot}$ and an initial radial extension from 4 out to 100 au. The gas surface density profile follows $\Sigma \propto r^{-1}$, and we adopt a locally isothermal equation of state, with a temperature profile given by $T \propto r^{-0.5}$. The disc aspect ratio is initially set to $H/R = 0.057(R/R_{ref})^{0.25}$, where the reference radius is $R_{ref} = 30$ au. We follow the Shakura & Sunyaev (1973) prescription for α by fixing $\alpha_{SS} = 0.005$ at our chosen resolution, and with a corresponding alpha viscosity parameter $\alpha_{av} \approx 0.2$ (Lodato & Price 2010).

For Section 3.3, we also include a population of 1-mm dust grains. We compute the dust dynamics using the one-fluid algorithm (Laibe & Price 2014; Price & Laibe 2015; Ballabio et al. 2018). We initially set the dust radial density profile equal to the gas profile, with a gas-to-dust ratio of 100.

In order to compare our model with observations of HD 143006, we post-process our simulations using the Monte Carlo radiative transfer code MCFOST (Pinte et al. 2006, 2009). The code uses a Voronoi mesh where each cell corresponds to the position of an SPH particle. We use 10^8 photon packets to compute the dust temperature. We attribute the known stellar parameters to the primary star and calculate the radius from temperature and luminosity. We then assume a 5-Myr isochrone (Siess, Dufour & Forestini 2000) and derive the properties of the secondary star. The masses and positions are updated directly from the simulation. Fig. A1 in Appendix A shows a comparison between the temperature computed by MCFOST and assumed in PHANTOM.

We compute synthetic CO channel maps of the ^{12}CO $J = 2$–1 line (assuming a CO-to-H_2 abundance of 1×10^{-4}, $T_{gas} = T_{dust}$, and that the population levels are at LTE). The synthetic CO maps have a spectral resolution of ∼100 m s^{-1}. We also compute the corresponding simulated IR scattered light and 1.3-mm continuum images. For this calculation, we consider a population of grains with size ranging from 0.03 to 1000 μm. Dust grains smaller than 1 μm are assumed to follow the gas distribution, and in each cell we compute the density for each grain size by interpolating the SPH densities between 1 μm and 1 mm. The grain size distribution over the whole disc is then normalized following a power law d$n(a) \propto a^{-3.5}$ da, and a dust-to-gas ratio of 100. The dust optical properties are

determined using the Mie theory. Following Benisty et al. (2018), we convolve the IR image with an angular resolution of ∼0.037 arcsec. We then perform synthetic observations of the sub-mm flux, using the software CASA (McMullin et al. 2007). We use an integration time of 35 min and a beam size of ∼52 × 45 mas consistent with the observations, using the corresponding preset configuration. We measure an RMS noise of ∼6.2×10^{-2} mJy per beam.

3 MODELS

We investigate three different scenarios in turn, as motivated by the features observed in HD 143006: (i) an inclined inner binary, (ii) a misaligned planet around a single star, and (iii) an inclined binary with a co-planar planet. A snapshot of a simulation for each scenario is shown in Fig. 1. The first, second, and third columns correspond to the cases presented in Sections 3.1, 3.2, and 3.3, respectively. The success of each scenario is measured by comparison with the observed features. We present the density evolution and synthetic observations only for our final model.

3.1 An inclined binary

We first test the possibility that the misalignment of the central region is driven by an inclined binary system, as suggested in Benisty et al. (2018) based on Facchini et al. (2018).

Taking into consideration the detection limits of NIR observations (see Section 1), we perform a set of hydrodynamic simulations with a gaseous disc and a central binary of mass ratio $q = 0.1$, 0.2, 0.3 and separation $a = 1$, 2, and 5 au. The binary is initialized on a circular orbit, inclined by 60° to the disc plane. Here, we deliberately choose a large inclination for the binary as Facchini et al. (2018) showed that this larger inclination guarantees a wide range of relative misalignments, including the 30–40° suggested by the observations as Benisty et al. (2018). We let the system evolve for a few thousand binary orbits and consider the resulting disc structure.

As predicted with equation (9) of Nixon et al. (2013), we find that the disc breaks at the expected radius in our simulations with $a = 2$ or 5 au and $q = 0.2$ or 0.3. In particular, in the simulation with $a = 2$ au and $q = 0.2$ the disc breaks at roughly 8 au, which corresponds to the upper limit in the observations. A snapshot from this simulation is shown in the left-hand panels of Fig. 1, after about 2000 binary orbits. None of these simulations produce the extended dust gap or explain the kink in the channel map found around 32 au. We thus conclude that a misaligned binary is not sufficient to explain the observed morphology of HD 143006.

3.2 A misaligned planet around a single star

Our second scenario considers an inclined companion orbiting around a single star that can tilt the inner disc casting a shadow on to the outer disc. We therefore model a disc around a single star of mass 1.8 $M_\odot$ and a misaligned planet at $R_p = 32$ au. We consider inclinations of 15° and 30° and four planetary masses, $M_p = 2$, 5, 10, and 20 $M_{\rm Jup}$. We initialize the disc with a gap of width $\Delta r = 2$ au, centred around the location of the planet, to prevent unphysically rapid gas accretion at the beginning of the simulation. For this model, we evolved the hydrodynamic simulations for ∼300 orbits of the planet and then we computed the CO channel maps. All the considered planets are massive enough to leave a signature above the detection limit of the kinematic observations.

Looking at the results of our hydrodynamic simulations, we find that planets with masses of 2 and 5 $M_{\rm Jup}$ produce a maximum

relative misalignment between inner and outer disc of 4°, while the 10 $M_{\rm Jup}$ planet reaches a relative misalignment of about 12°. Only the 20 Jupiter-mass planet on a 30° inclined orbit produces the large relative misalignment between inner and outer discs required by the scattered light observations. Indeed, after about 100 orbits of the planet, we measure a relative misalignment of 30°. However, the planet's angular momentum exceeds the angular momentum of both the inner and outer disc. As a result, the outer disc also moves in response to the planet, tilting away from its initial position and aligning with the rest of the disc. The middle panels of Fig. 1 show a snapshot of the 20 Jupiter-mass planet inclined by 30° after orbiting ∼195 orbits. Thus, a planet massive enough to make the required misalignment between the inner and outer disc is also massive enough to tilt the outer disc, and as such the misalignment is not sustainable on time-scales greater than about 200 planet orbits.

In all of our misaligned planet simulations that develop an inclined inner disc, because the inner and outer disc are separated at the orbit of the planet all of the material interior to the planet orbit becomes misaligned. This results in a velocity perturbation that is visible in the simulated channel maps at all radii $r \leq R_p$. An example is illustrated in Fig. 2. However, fig. 7 in Pérez et al. (2018) shows only a kink in the redshifted channel, at the azimuthal and radial position of the planet. No other deviations or evidence of misalignment from the Keplerian pattern are visible. While a misaligned planet may lead to a misaligned inner disc, the suggested location of the planet and indication of where the disc is misaligned are not consistent with this idea. We therefore conclude that a misaligned planet only is also not able to explain all of the features in HD 143006.

3.3 An inclined binary with a planetary companion

As the previous two scenarios cannot explain the data, we propose a third option: an inclined binary with an outer planetary companion. As mentioned in Section 3.1, an inclined binary can warp the disc, breaking and driving precession of the inner disc. The planet instead is able to open a gap in the outer region of the disc. We thus seek to combine elements of these previous scenarios to simultaneously explain all the features identified in HD 143006. For this calculation, we select the most promising parameters from previous simulations. We adopted a binary separation of 2 au, a mass ratio 0.2, and an orbital inclination of 60°. We embedded a planet at 32 au with mass 10 $M_{\rm Jup}$, on an orbit co-planar with the outer disc. For this scenario only we additionally included a dust component, described in Section 2.

Fig. 3 shows a face-on (upper panel) and edge-on (lower panel) density rendered view of this planet-hosting disc with a central misaligned binary. As in Section 3.1, we find that after a few hundred years, the inner disc breaks and start precessing away from the outer disc.

We derive the precession time by measuring how long it takes for the disc to twist through a full 2π radians. Following Nealon, Price & Nixon (2015, equation A2 in the appendix), we measure the gradient of the twist and find that the precession time-scale increases from 400 yr at 1000 yr to 1300 yr at 3500 yr. The precession slows down as the inner disc tends to align with the binary orbit. We find a similar result when using equation (4) in Facchini et al. (2018). This relationship is very sensitive to the inner edge of the disc, and for an inner radius of 4 au we derive a precession time-scale of ∼1100 yr. Likewise, we calculate the precession time of the outer disc, which is much slower, and find that it is ∼1.7×10^5 yr.

After approximately 50 planetary orbits, an annular dust gap has formed within the disc, extending out to 40 au. The disc remains stable for about hundred orbits of the planet. Considering that
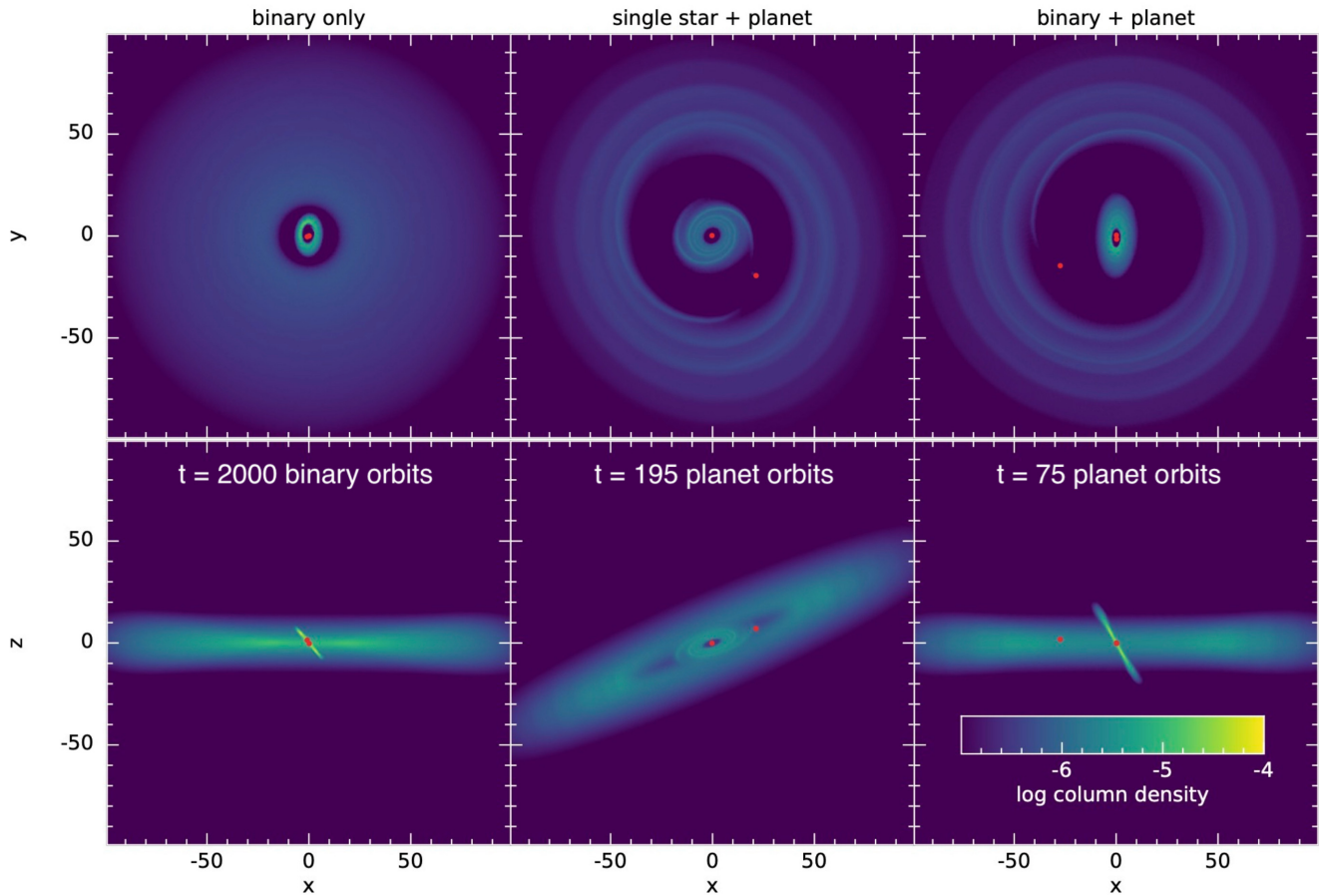
Figure 1. Snapshots of the hydrodynamic simulations for the three scenarios presented in Section 3: a binary inclined by $60°$, with $q = 0.2$ and $a = 2$ au (first column), a 20 Jupiter-mass planet located at $R_p = 32$ au around a single star and misaligned by $30°$ (second column), and a planet orbiting an inclined binary, where we combine the properties of the previous configurations (third column). The first and second rows show a face-on and an edge-on view of the gas density distribution, respectively. The sink particles are indicated by the red dots. We have chosen a representative physical time for each situation.
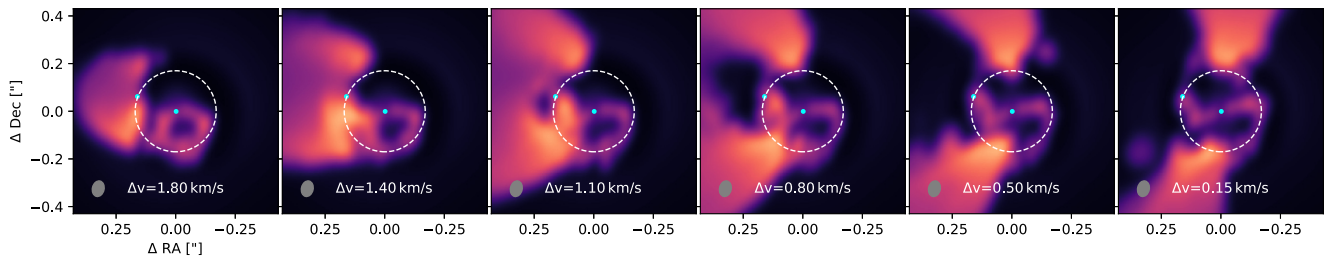
Figure 2. Redshifted channel maps of the ^{12}CO $J = 2–1$ emission for the 'single star + planet' model, calculated subtracting the systemic velocity. Here, we show the results from the modelling presented in Section 3.2. The cyan dots indicate the position of the central star and the 20 M_{Jup} planet, inclined by $30°$ to the outer disc. The gas velocity pattern is perturbed by the misaligned material interior to the planet's orbit (indicated by the dashed white circle). The beam size is represented by the grey ellipse in the bottom left corner of each channel.

circumbinary orbits are generally stable especially far from the centre and the planet is not massive, we expect the system to survive in this configuration also on a longer time-scale. Holman & Wiegert (1999) have investigated the long-term stability of planets in binary systems. In particular, they derived the critical semimajor axis beyond which orbits are dynamically stable. Interestingly, when considering P-type planets, non-co-planar orbits, such as polar, are stable over a wide range of binary properties (Cuello & Giuppone 2019; Chen, Lubow & Martin 2020). We note, however, that if the planet is massive enough and close to the central star, it can cause the binary to precess (e.g.

Chen et al. 2019; Cuello & Giuppone 2019). During the simulation, a fraction of the disc mass is also accreted on to the planet, forming a circumplanetary disc, misaligned to the orbital plane.

3.4 Synthetic observations

3.4.1 'Choosing' the observed configuration

Observable features such as shadows and kinks depend on the relative phases of inner/outer disc precession, and also on the phases of the
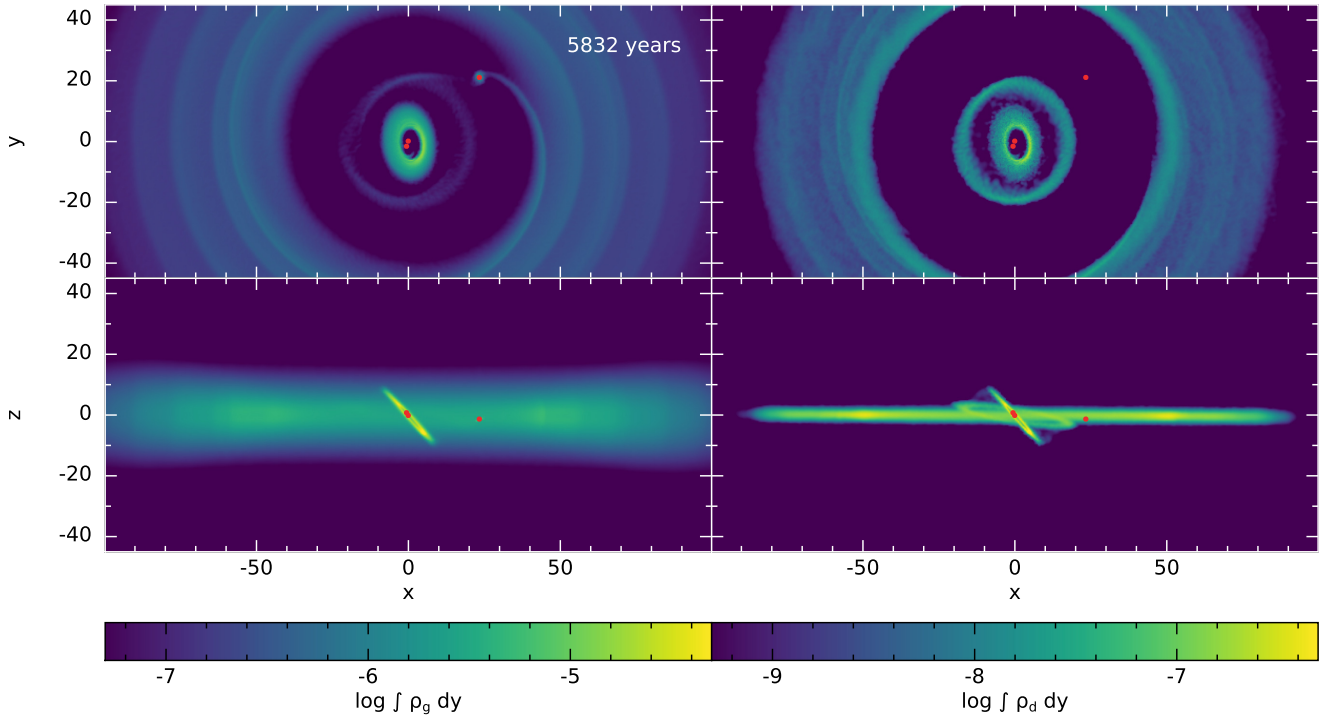
Figure 3. Snapshots of the 'binary + planet' hydrodynamic simulations, showing a face-on (upper panels) and an edge-on view (lower panels) of a planet hosting disc, with a misaligned central binary. We present the gas and dust surface density profiles in the left and right columns, respectively. The red dots represent the sink particles in our simulation.

planet and binary orbits. We therefore only expect to reproduce these observations at particular times in our simulation, when all these phases are similar to the current configuration of the HD143006 system. There are effectively two angles that determine the key observables: the relative misalignment between the inner and outer disc; and the orbital phase of the planet. The orientation of the inner disc primarily affects the IR scattered light and mm continuum emission, while the position of the planet determines the location of the kink in the CO channel maps.

The evolution of the relative misalignment between the inner and outer discs is shown in Fig. 4. Once it breaks, the inner disc completes several full precessions during the course of the simulation, and the relative misalignment is gradually damped as the inner disc aligns with the binary (which, as discussed in Section 3.1, was initially inclined at $60°$). If the binary is eccentric and misaligned, the inner disc could become polar (Aly et al. 2015; Martin & Lubow 2017, 2018; Zhang et al. 2018; Cuello & Giuppone 2019). If this happens, then the mutual misalignment between the three components is long lived. The best match with the observed misalignment is therefore found close to the minimum of each precession cycle. As we have not fine-tuned the simulation parameters there is no 'perfect' snapshot that reproduces all of the observations precisely, but we see closest agreement at several different times during the simulation. Our model also relies on the dust clearing between 8 and 30 au by the planet. This gap has mostly been cleared by $t \sim 7000$ yr, so we restrict our choice to later times in the simulation. We therefore choose to show results from the configuration at $t = 5832$ yr (shown in Fig. 3): this time represents the 'best compromise' in matching the observations. It corresponds to 43 orbits of the planet and 2766 binary orbits. At this time, the inner disc has a relative inclination of $\simeq 47°$ with respect to the outer disc, which is consistent with
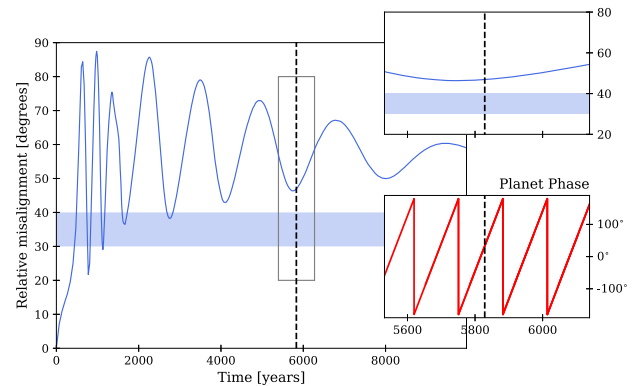

Figure 4. Time evolution of the relative misalignment between inner and outer discs. The shaded blue area represents the range of relative inclinations inferred from observations of HD143006 (Benisty et al. 2018). The upper inset is a zoom in of the relative misalignment in the time period highlighted by the grey rectangle. The lower inset shows the planet's orbital phase (expressed in degrees) over the same time period. The dashed black vertical line at $t = 5832$ yr indicates the time at which we select the snapshot shown in Fig. 3.

the IR scattered light observations (Benisty et al. 2018), and the continuum emission and CO velocity field (Pérez et al. 2018). Additionally, the planet is located at the approximate location of the kink suggested by Pérez et al. (2018) and confirmed by Pinte et al. (2020). Using this configuration of the system, as shown in Fig. 3, we now consider the different synthetic observations in turn.
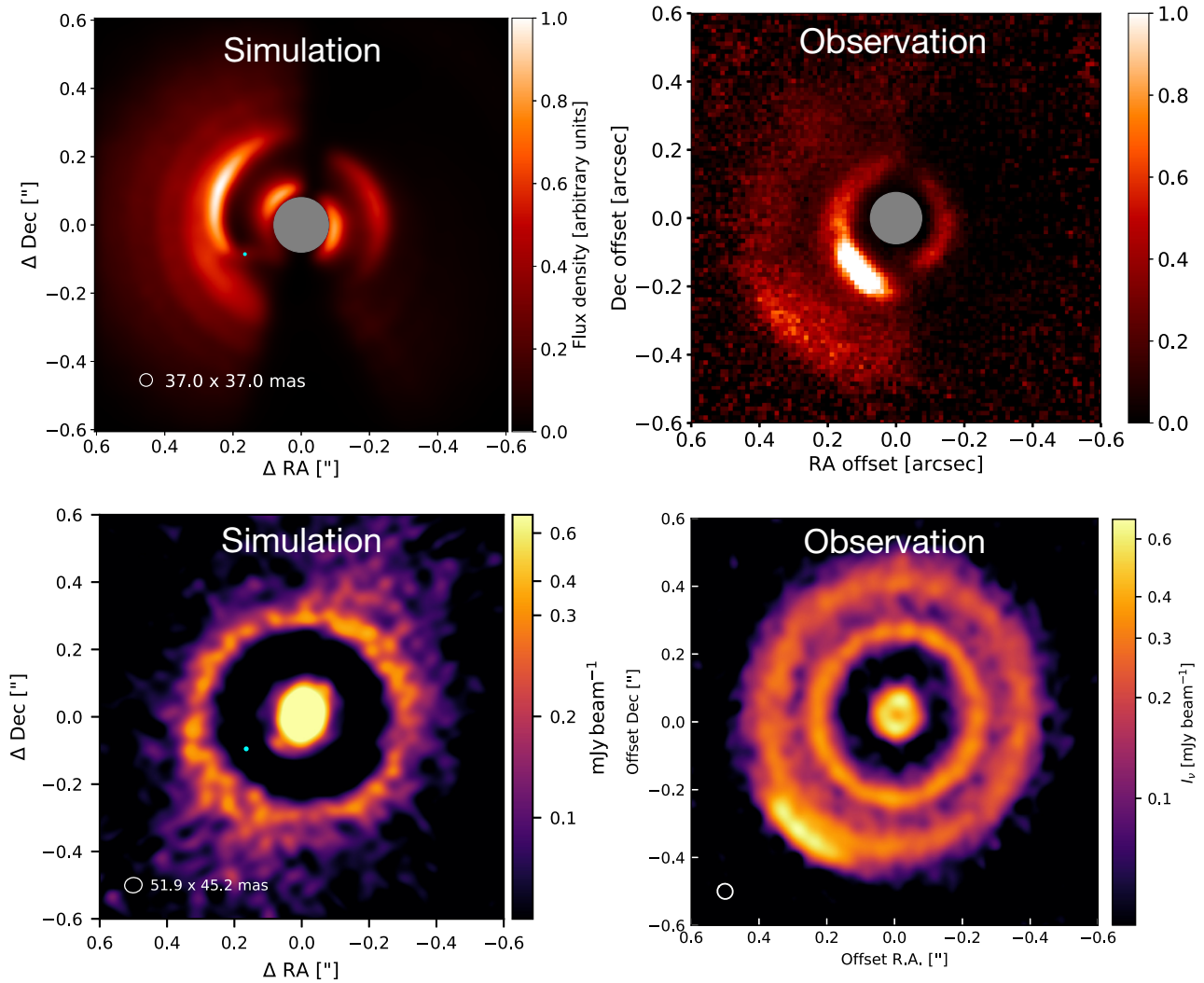
Figure 5. Comparison between the results from our 'binary + planet' model (left-hand panels) and the observations (right-hand panels). Top panels: Polarized intensity image Q_Φ observed at 1.2 μm (*J* band) of the hydro simulation of HD 143006. The flux has been scaled by r^2 to enhance the drop in intensity. The grey circle indicates the 0.08 arcsec coronographic mask. The image on the right has been taken from Benisty et al. (2018).[1] Bottom panels: ALMA Band 6 synthetic observation at 1.3 mm of the dust continuum emission. The empty circles in the bottom left corners indicate the corresponding beam size. The image on the right has been taken from Pérez et al. (2018).[2]

3.4.2 Infrared emission

We computed synthetic observations from our hydrodynamic simulation of HD 143006 with both the binary and the planet. In the upper left panel of Fig. 5, we present a synthetic scattered light observation at 1.2 μm (*J* band). Following Benisty et al. (2018), the flux has been scaled by r^2 to enhance the drop in intensity, along with a coronographic mask. The image shows a left/right brightness asymmetry, along with a bright arc due to the illumination of the inner edge of the outer disc. The misaligned inner disc obscures the light from the central binary on one side of the disc, causing the wide shadow across half the disc. This is accompanied by two narrow-lane shadows cast by the mid-plane of the inner disc. The two smaller arcs closest to the coronographic mask are caused by an illumination effect of the material around the inner disc, which has not fully accreted on to the inner disc (as shown in Fig. 3). Our simulations show that this feature disappears after ∼7000 yr, once the dust has accreted on to the central disc.

3.4.3 CO kinematics

Fig. 6 shows our synthetic velocity channel maps for the CO emission. The overlaid white contours are the kinematic detections as presented in fig. 7 of Pérez et al. (2018). The velocity in each channel is calculated relative to the systemic velocity. Top and bottom rows show the blueshifted and redshifted channels, respectively. A kink is visible in some of the redshifted channels, and coincides with the radial and azimuthal position of the planet (indicated in cyan). This observational signature has been previously attributed to the presence of a Jupiter-mass planet within the disc (e.g. Pinte et al. 2019, 2020), and it is confirmed by the model presented here. We also notice an asymmetry in the wings of the butterfly shaped flux distribution, which can also be traced in the observations in fig. 7 of Pérez et al. (2018). In this context, the stellar companion could also be responsible for a perturbation of the velocity pattern. These effects could not be easy to disentangle from other perturbations, especially considering the lower resolution of the CO observations.
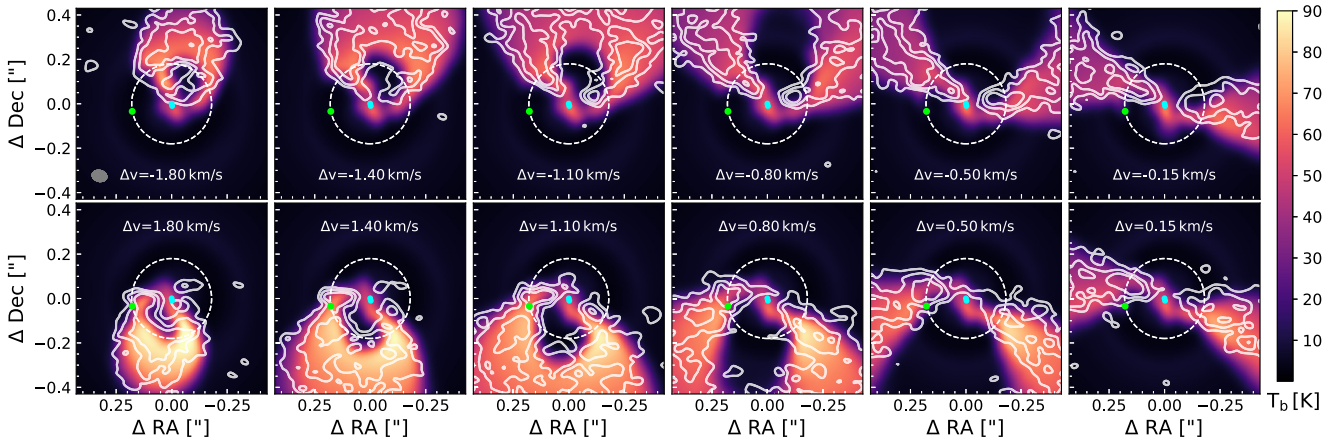
Figure 6. Synthetic channel maps of the ^{12}CO $J = 2$–1 emission, calculated subtracting the systemic velocity. Top and bottom rows are the blueshifted and redshifted channels, respectively. The overlaid white contours are the kinematic observations as presented in fig. 7 of Pérez et al. (2018). The cyan dots indicate the positions of the central binary, while the green dot and the white dashed circle indicate the position and orbit of the planet. The beam resolution of 66×49 mas is represented by a grey ellipse in the top left panel. The spectral resolution is 100 m s^{-1}.

None the less, we expect these effects to be very close to the central binary.

3.4.4 Sub-mm dust emission

Finally, we compute the dust temperature structure using MCFOST and produce a continuum image at 1.3 mm (240 GHz). In contrast to the IR scattered light observations, much of the disc is optically thin in mm continuum emission, so these observations primarily trace the disc mid-plane. The lower left panel of Fig. 5 shows a synthetic Band 6 ALMA map, calculated using the CASA software (McMullin et al. 2007). The 10 $M_{\rm Jup}$ embedded planet at 32 au is massive enough to open a gap in the dust. The large annular dust gap is detected in the sub-mm observations and can also be seen in our simulations (see lower right panel of Fig. 5). We additionally compute a Band 6 synthetic observation of a snapshot from the hydrodynamic simulation at about 1300 yr, using an integration time of 5 h and removing any noise. Fig. 7 shows the post-processed 1.3-mm dust emission where a circumplanetary disc is visible. The inset illustrates a zoom in on the circumplanetary disc itself, with the contours indicating the emission at 0.05, 0.75, 0.1, and 0.15 mJy per beam.

4 DISCUSSION

We aimed to provide a dynamical explanation for the substructures in the HD 143006 disc. We have shown that a central misaligned binary and an embedded planetary companion is the minimal configuration necessary.

If confirmed, this would be the first known example of a circumbinary planet that is significantly misaligned to the binary orbital plane. Jorquera et al. (2021) have investigated the possible presence of a planetary companion within the gap of HD 143006. Using high contrast direct imaging observations carried out with NaCo/VLT, they were however unable to resolve any Jupiter-mass planet below 50 au, at the distance of Upper Sco.

The HD 98800 system hosts a protoplanetary disc that orbits a binary in a polar configuration (Kennedy et al. 2019), stable enough to form misaligned planets. However, no planets have been currently detected within HD 98800. To date, 14 transiting
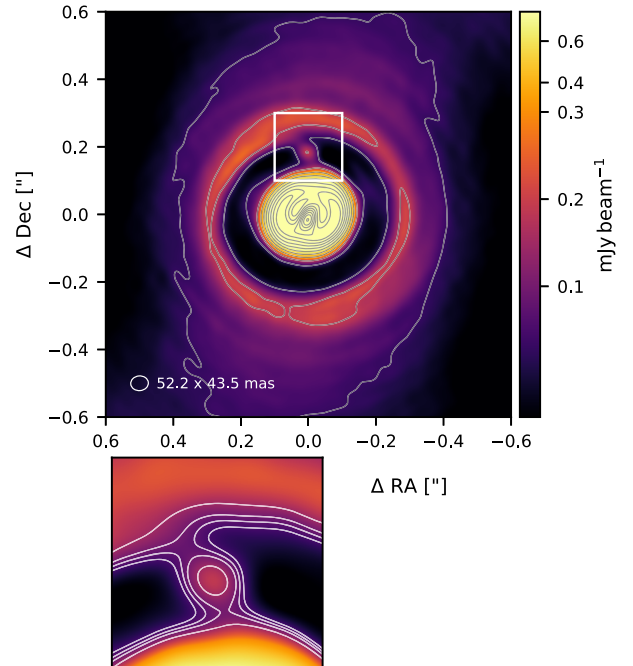

Figure 7. ALMA Band 6 synthetic observation at 1.3 mm of the dust continuum. The image was obtained post-processing an earlier dump compared to the one used in Fig. 5, over an integration time of 5 h and removing any noise. The grey contours go from 0.03 up to 3.0 mJy per beam, over 20 bins. The white rectangle indicates the region shown in the inset. The contours in the inset correspond to 0.05, 0.075, 0.1, and 0.15 mJy per beam.

circumbinary planets are known, and they are all co-planar, within a few degrees, with the binary orbit (Kostov et al. 2020). The frequency of aligned planetary companions is consistent with the occurrence rate of equivalent planets around single stars. If, however, inclined circumbinary planets are common, the inferred occurrence rate increases substantially (Armstrong et al. 2014). Detecting circumbinary planets through the transit method is, however, very challenging. It is particularly hard to obtain a regular transit where the planet passes in front of both stars (Martin & Triaud 2014).

HD143006 adds to a growing collection of discs suggested to contain misaligned central binaries, including HD 142527 (Lacour et al. 2016; Price et al. 2018b), GW Ori (Kraus et al. 2020), AB Aur (Poblete, Cuello & Cuadra 2019; Poblete et al. 2020), and HD 98800 (Kennedy et al. 2019) to name a few.

4.1 Misaligned circumplanetary disc

During giant planet formation, a subdisc forms around the Jovian-mass planet. Such circumplanetary discs regulate the accretion on to the planet and are the origin of satellites (e.g. Szulágyi et al. 2014; Szulágyi, Mayer & Quinn 2017). Our hydrodynamic simulations of HD 143006 show the formation of a circumplanetary disc around the 10 Jupiter mass planet. This disc is not co-planar with the orbit of the planet, or with the outer disc. The interaction with the misaligned inner binary, and possibly the misaligned inner disc, produces a significant tilt of the circumplanetary disc. Even with a $10\,M_{\rm Jup}$ planet, the disc around such a planet is unlikely to have been identified in existing observations as the detection of circumplanetary discs requires deep observations at high resolution (Szulágyi et al. 2018; Zhu, Andrews & Isella 2018). In the case of HD 143006, the ALMA observations are limited by the telescope resolution and integration time (Pérez et al. 2018) therefore if existent, such circumplanetary disc would have remained undetected. We derived an estimate of the flux of the circumplanetary disc and find that the emission peaks at $\sim$0.1–0.15 mJy per beam. This result shows that under ideal circumstances (i.e. no noise, 5 h of integration time) the circumplanetary disc may be bright enough to be detectable.

Recently, Martin, Zhu & Armitage (2020) investigated the conditions under which the tilt of a circumplanetary disc can grow, arguing that a rapid growth is typically favoured. This could potentially have implications for both satellites formation and additionally the observability of circumplanetary discs.

4.2 Observational predictions

4.2.1 Disc-induced features

We can calculate the precession time-scale for both the inner and outer discs. As shown in Section 3.3, we find that the inner disc precesses $\sim 10^2$ times faster than the material at larger radii. Assuming that the inner disc is still misaligned to the binary, this implies that the observed narrow-lane shadows should precess on a time-scale much shorter than the overbrightness detected at larger radii. The apparent motion of the shadow cast by the precessing inner disc is complex, and depends sensitively on the (unknown) orbital phases (Nealon et al. 2020). However, the inner disc precession rate of $\sim$0.3° yr^{-1} suggests this could potentially be detected on a time-scale of $\lesssim$10 yr. Eventually, the inner disc will stop precessing and align with the binary. Under these circumstances, the produced shadows will not move.

4.2.2 Planet-induced features

The orbital period of the planet embedded at 32 au is approximately 135 yr, 10 times faster than the precession time-scale for the inner disc. This means that the planet advances on its orbit by $\sim$3° yr^{-1}. Therefore, when looking at observational predictions for the planet we expect to see a variation on a relatively short time. The resolution of the current CO observations corresponds to $\sim$10–15° of orbital motion at the planet's position. Changes to the perturbation (kink) in the channel maps may therefore be detectable within 5–10 yr.

Although weakly shown in Fig. 5, we additionally detect a shadow induced by the planet in the scattered light image. The planet and its disc are indeed able to cast a small shadow on to the outer disc, at the edge of the gap. The time variability of this illumination effect is again relatively short and, considering that scattered light observations have higher resolution, we expect to be able to detect any significant change within the next few years.

4.3 Caveats

Our model successfully reproduces the major features in the scattered light observations and the CO kinematics, but does not match some of the mm continuum features seen with ALMA. In particular, the formation of a secondary shallow gap at larger radii ($\sim$51 au; Pérez et al. 2018) is difficult to achieve with a single planet located at 32 au. Dong et al. (2017) showed that a super-Earth is able to open a double gap and such gaps are expected to be shallower. However, this mechanism requires a much lower disc viscosity ($\alpha \lesssim 10^{-4}$) than is used here. Another scenario that does not require an additional body is offered by the work presented in Aly & Lodato (2020). They have studied the formation of a warp induced by differential precession of a gas + dust disc around a binary. Due to the relative velocity between gas and dust, dust particles pile up at the warp location and generate dusty rings. Alternatively, a second smaller planet located at larger radii is in principle able to open a shallower gap, despite not being detected in the CO emission. None the less, adding an extra body would result in an even more complicated scenario, and the long-term stability of such a system is not clear.

The bright arc in the south-east direction is also hard to reproduce. When considering fig. 1 in Pérez et al. (2018), the peak of the asymmetric structure at $\sim$74 au is bright enough to require dust trapping. They model this arc using a prescription for a dust vortex, but this interpretation again requires very low viscosity (e.g Lyra et al. 2009; Zhu & Stone 2014). Future work using a lower viscosity than we have employed here may resolve this discrepancy. Our simulations are also limited by the radial extent of the disc, which is initially set to 100 au. The choice of outer radius influences the development and appearance of sub-structures in the outer disc. For our chosen outer radius and computational time of our simulation, the outer disc is still yet to reach a steady state. This potentially explains the lack of substructure at larger radii.

Despite these limitations, our model is able to correctly predict the formation of a clear annular gap. If we want to be more precise, the simulations slightly overpredict the radial width of the gap, as shown in the bottom panels of Fig. 5. A more extensive study exploring a lower mass planet, a higher disc viscosity and/or a higher disc aspect ratio (Crida, Morbidelli & Masset 2006), would be needed to help minimize the gap width and obtain a closer match with the observation.

We stress that we have not explored a large range of model parameters in order to find the closest match to the observations. Instead this study is a proof of concept. Our results show that a relatively simple model – an inclined binary and an embedded planet – can explain the key observed sub-structures in HD 143006.

5 CONCLUSIONS

We investigate three possible configurations that could explain the substructures observed in HD 143006. Using 3D hydrodynamic simulations we model the disc and computing synthetic observations we compare our results with the current data (Andrews et al. 2018; Benisty et al. 2018; Pérez et al. 2018)

We first considered an inclined binary, which breaks and tilts the disc. This configuration can reproduce part of the features detected in HD 143006, specifically the shadowing effects (i), seen in scattered light (see Section 1). The misaligned binary can also drive a relative misalignment that matches the one measured from the observations (iii). This model, however, fails in reproducing both the annular dust gap observed in the mm continuum and the kink seen in the channel maps. In fact, the mm observation and CO channel maps suggest the presence of a planet further out in the disc. We then examined an embedded planetary companion orbiting on an inclined orbit around a single star. When looking at the kinematics, even a small planet leaves a trace detectable in the channel maps (vi). However, the misaligned planet is massive enough to break the disc into two and to misalign the disc material interior to its orbit. The newly formed misaligned inner disc produces a perturbation in the gas velocity pattern that is not detected in the channel maps.

We therefore propose a third possibility, involving both a misaligned central binary and an embedded planet aligned with the outer disc. Our model reproduces the main features inside 40 au in the scattered light image, channel maps, and ALMA observations. We thus conclude that the minimum configuration for HD 143006 requires an inner, misaligned binary and a planet co-planar with the disc. We suggest $\sim$3–10 $M_{\rm Jup}$ planet located at 32 au within the dust gap. Additionally, our study predicts the presence of a kink at the planet's location. This result confirms previous findings by both Pérez et al. (2018) and Pinte et al. (2020), and helps constraining the mass and location of the planet in HD 143006. Current direct imaging observations are not sensitive to the proposed planet (Jorquera et al. 2021). Future observations at higher angular resolution (i.e. with SPHERE or MUSE) might be able to detect such a massive planet and ultimately verify our findings. If confirmed, to our knowledge this would be the first case of a misaligned circumbinary planet.

DATA AVAILABILITY

The data underlying this article will be shared on reasonable request to the corresponding author. The code PHANTOM used in this work is publicly available at https://github.com/danieljprice/phantom, as well as the code MCFOST, which is available upon request. The software CASA is also public and can be downloaded from https://casa.nrao.edu/casa_obtaining.shtml.

REFERENCES

ALMA Partnership, 2015, ApJ, 808, L3
Aly H., Lodato G., 2020, MNRAS, 492, 3306
Aly H., Dehnen W., Nixon C., King A., 2015, MNRAS, 449, 65
Andrews S. M., 2020, ARA&A, 58, 483
Andrews S. M. et al., 2018, ApJ, 869, L41
Armstrong D. J., Osborn H. P., Brown D. J. A., Faedi F., Gómez Maqueo Chew Y., Martin D. V., Pollacco D., Udry S., 2014, MNRAS, 444, 1873
Ballabio G., Dipierro G., Veronesi B., Lodato G., Hutchison M., Laibe G., Price D. J., 2018, MNRAS, 477, 2766
Benisty M. et al., 2018, A&A, 619, A171
Chen C., Franchini A., Lubow S. H., Martin R. G., 2019, MNRAS, 490, 5634
Chen C., Lubow S. H., Martin R. G., 2020, MNRAS, 494, 4645
Crida A., Morbidelli A., Masset F., 2006, Icarus, 181, 587
Cuello N., Giuppone C. A., 2019, A&A, 628, A119
Dong R., Li S., Chiang E., Li H., 2017, ApJ, 843, 127
Facchini S., Lodato G., Price D. J., 2013, MNRAS, 433, 2142
Facchini S., Juhász A., Lodato G., 2018, MNRAS, 473, 4459
Francis L., van der Marel N., 2020, ApJ, 892, 111
Gaia Collaboration, 2018, A&A, 616, A1
Holman M. J., Wiegert P. A., 1999, AJ, 117, 621
Holman M., Touma J., Tremaine S., 1997, Nature, 386, 254
Hunter J. D., 2007, Comput. Sci. Eng., 9, 90
Jorquera S. et al., 2021, AJ, 161, 146
Kennedy G. M. et al., 2019, Nat. Astron., 3, 230
Kostov V. B. et al., 2020, AJ, 159, 253
Kraus A. L., Ireland M. J., Martinache F., Lloyd J. P., 2008, ApJ, 679, 762
Kraus S. et al., 2020, Science, 369, 1233
Lacour S. et al., 2016, A&A, 590, A90
Laibe G., Price D. J., 2014, MNRAS, 440, 2136
Lodato G., Price D. J., 2010, MNRAS, 405, 1212
Lyra W., Johansen A., Klahr H., Piskunov N., 2009, A&A, 493, 1125
Martin R. G., Lubow S. H., 2017, ApJ, 835, L28
Martin R. G., Lubow S. H., 2018, MNRAS, 479, 1297
Martin D. V., Triaud A. H. M. J., 2014, A&A, 570, A91
Martin R. G., Zhu Z., Armitage P. J., 2020, ApJ, 898, L26
Marzari F., Thebault P., 2019, Galaxies, 7, 84
McMullin J. P., Waters B., Schiebel D., Young W., Golap K., 2007, in Shaw R. A., Hill F., Bell D. J., eds, ASP Conf. Ser. Vol. 376, Astronomical Data Analysis Software and Systems XVI. Astron. Soc. Pac., San Francisco, p. 127
Montesinos M., Cuello N., 2018, MNRAS, 475, L35
Nealon R., Price D. J., Nixon C. J., 2015, MNRAS, 448, 1526
Nealon R., Pinte C., Alexander R., Mentiplay D., Dipierro G., 2019, MNRAS, 484, 4951
Nealon R., Price D. J., Pinte C., 2020, MNRAS, 493, L143
Nixon C., King A., Price D., 2013, MNRAS, 434, 1946
Pecaut M. J., Mamajek E. E., Bubar E. J., 2012, ApJ, 746, 154
Pérez L. M. et al., 2018, ApJ, 869, L50
Pinte C., Ménard F., Duchêne G., Bastien P., 2006, A&A, 459, 797
Pinte C., Harries T. J., Min M., Watson A. M., Dullemond C. P., Woitke P., Ménard F., Durán-Rojas M. C., 2009, A&A, 498, 967
Pinte C. et al., 2019, Nat. Astron., 3, 1109
Pinte C. et al., 2020, ApJ, 890, L9
Poblete P. P., Cuello N., Cuadra J., 2019, MNRAS, 489, 2204
Poblete P. P. et al., 2020, MNRAS, 496, 2362
Price D. J., 2007, PASA, 24, 159
Price D. J., Laibe G., 2015, MNRAS, 451, 813
Price D. J. et al., 2018a, PASA, 35, e031
Price D. J. et al., 2018b, MNRAS, 477, 1270
Quarles B., Li G., Kostov V., Haghighipour N., 2020, AJ, 159, 80

Shakura N. I., Sunyaev R. A., 1973, A&A, 24, 337
Siess L., Dufour E., Forestini M., 2000, A&A, 358, 593
Szulágyi J., Morbidelli A., Crida A., Masset F., 2014, ApJ, 782, 65
Szulágyi J., Mayer L., Quinn T., 2017, MNRAS, 464, 3158
Szulágyi J., Plas G. v. d., Meyer M. R., Pohl A., Quanz S. P., Mayer L.,
    Daemgen S., Tamburello V., 2018, MNRAS, 473, 3573
Zhang S. et al., 2018, ApJ, 869, L47
Zhu Z., Stone J. M., 2014, ApJ, 795, 53
Zhu Z., Andrews S. M., Isella A., 2018, MNRAS, 479, 1850

APPENDIX A: TEMPERATURE STRUCTURE

Nealon et al. (2019) have previously investigated a possible discrepancy between the adopted radial temperature profile and the vertical scale-height derived in MCFOST. We perform the same analysis, where we extract and average the temperature of those Voronoi cells that are within $|z| < 0.03$ from the warped mid-plane. The temperature obtained from the MCFOST calculations is consistent with the locally isothermal approximation used in the hydrodynamic simulations to within the error bars across most of the radial extent of the disc, as shown in Fig. A1. We note that in the gap ($\sim 32 \pm 5$ au) the gas density is negligible, so we do not plot the temperature in this region.
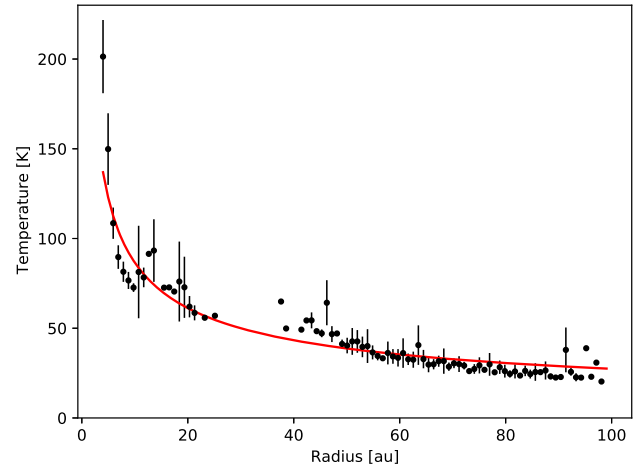

Figure A1. Comparison between the mid-plane temperature structure calculated by MCFOST, used to produce the synthetic images (black points, with error bars indicating the standard deviation), and the vertically isothermal approximation adopted in SPH (red line).

This paper has been typeset from a TEX/LATEX file prepared by the author.